doi.org/10.1002/cnma.202300619

# Synthesis and Properties of Ag-Au Alloy Nanoparticles with Controlled Composition for Computed Tomography Imaging Applications

Nguyen Thi Ngoc Linh,[a] Le The Tam,*[b] Nguyen Hoa Du,[b] Nguyen Dinh Vinh,[a] Phan Thi Hong Tuyet,[b] Bui Minh Quy,[a] Cao Thu An,[c] Nguyen Thi Suong,[b] Nguyen Thi Hong Hoa,[a] and Le Trong Lu[d, e]

Numerous non-invasive assays have been developed to support CT imaging, consequently increasing the precision of diagnosis. Although these efforts made a significant contribution to clinical research, there is still more to be done. The goal is to replace conventional contrast agents with more potent ones. In this study, Ag–Au alloy nanoparticles were fabricated by substitution method between the precursor $Au^{3+}$ and the previously prepared Ag nanoparticles. Effects of $Au^{3+}$ quantity on the formation and characteristics of Ag–Au alloy nanoparticles were investigated. It showed that Ag–Au nanoalloy with a size of 14.2 ± 1.0 nm, SPR absorption peak at 520 nm, and Ag: Au atomic ratio of approximately 3:1 were appropriate for biomedical applications. After phase transfer using poly (maleic anhydride-alt-1-octadecene) (PMAO), the nano Ag–Au solution owned remarkable durability, stability and non-toxicity Vero healthy cell line at high test concentration. *In-vitro* CT imaging demonstrated a good X-ray adsorption coefficient, and the hounsfield units (HU) was noticeably increased. As a promising CT contrast agent, the X-ray attenuation of nano Ag–Au solutions correlated linearly with concentrations. These findings led to a potential application in the biomedical field, particularly in computed tomography (CT) imaging diagnosis.

## Introduction

Recently, the precious metal nanoparticles (Ag, Au) have attracted many research interests.[1] Their applications primarily take advantage of their electrical conductivity, thermal conductivity, and especially surface plasmonic resonance. These precious nanoparticles absorb a wide range of visible light in the electromagnetic spectrum. The Au nanoparticles demonstrate inertness, stability, and low catalytic activity compared to silver nanoparticles. Thus, the synergistic effect of two components, Ag and Au, combined into an Ag–Au alloy would enhance the catalytic performance of separate nano-Ag or nano-Au. The alternation in structure and characteristics of the nano alloy Ag–Au suggest potential applications in biomedical such as antibacterial, imaging diagnosis, biolabelling, catalysis, drug delivery, cancer treatment, and biosensors.[2–5]

Imaging diagnosis utilizing computed tomography (CT) has been widely employed in medicine due to the high 3D spatial resolution, good image quality, and deep penetration of electromagnetic waves into bodies without surgery.[6] This approach requires short imaging time, thus especially suitable for emergency cases such as trauma. Low resolution and sensitivity are the fundamental drawbacks of CT imaging technology. Therefore, contrast agents are frequently used to improve the quality of CT images.[7,8] The compounds used as contrast agents for CT imaging cause X-ray attenuation by absorbing or diffracting X-ray radiations. Hence, contrast agents are often composed of high atomic number elements. The most commonly used contrast agents are iodine complexes such as Iohexol (commercial name as Omnipaque), Iodixanol (Visipaque), or Iversol (Iversol).[9,10] However, these complexes may cause many side effects, even death due to anaphylactic shock. Even though they do absorb X-ray radiation effectively, this type of contrast agent is not delivered to any specific diseases or tissues, and the pharmacokinetics is disposed of blood rapidly.[11] Iodine complexes are quickly removed from the blood circulatory system and primarily stored in the kidneys because of the short blood circulation duration. As a result, patients with kidney problems are not allowed to utilize these contrast agents.[12] Recent research has produced nanoparticles based on Au as an alternative for iodine complexes as a CT

---

[a] *Dr. N. T. N. Linh, Prof. N. D. Vinh, Dr. B. M. Quy, Dr. N. T. H. Hoa*
*Faculty of Chemistry*
*Thai Nguyen University of Sciences, Thai Nguyen University*
*Tan Thinh Ward, Thai Nguyen City (Vietnam)*

[b] *Dr. L. T. Tam, Prof. N. H. Du, Prof. P. T. H. Tuyet, N. T. Suong*
*School of Chemistry, Biology and Enviroment*
*Vinh University*
*182 Le Duan, Vinh City, Nghean (Vietnam)*
*E-mail: tamlt@vinhuni.edu.vn*

[c] *C. T. An*
*High School for the Gifted*
*Vinh University*
*182 Le Duan, Vinh City, Nghean (Vietnam)*

[d] *Dr. L. T. Lu*
*Institute for Tropical Technology,*
*Vietnam Academy of Science and Technology*
*18 Hoang Quoc Viet Road, Hanoi (Vietnam)*

[e] *Dr. L. T. Lu*
*Graduate University of Science and Technology*
*Vietnam Academy of Science and Technology*
*18 Hoang Quoc Viet Road, Hanoi (Vietnam)*

*Supporting information for this article is available on the WWW under https://doi.org/10.1002/cnma.202300619*

contrast agent.[13] The nano Au has a higher X-ray attenuation than iodine complexes due to its high atomic number (Z=79) and high electron density.[14] The surface properties of the nano Au may be easily changed by biocompatible ligands, and it is also chemically inert and highly biocompatible. Additionally, synthesis approaches can be used to tailor the size and shape of nano Au-based particles.[15] According to a number of studies, the size, surface charge, and coating of the Au nanoparticles could significantly affect how they were distributed in the body and how well they worked as CT contrast agents.[16–17] Dong et al.[18] have demonstrated that the Au nanoparticles (sample 4 with a size of 15 nm) produced considerable vascular contrast and increased the time for blood circulation. Using Au samples of bigger size (50–152 nm), little contrast was also found in blood vessels, indicating that larger particles were removed from the blood stream more quickly. Unfortunately, the high cost of gold nanoparticles prevents their broad uses in biomedicine. The current studies on Au nanoparticles and core-shell structures merely focus on their applications in photo-thermal therapy for cancer treatment.[19–21] Newly, the unique optical properties of Ag nanoparticles have been investigated as sensors, imaging agent and therapeutics.[22,23] The X radiation shielding property of Ag NPs meets the requirements for an alternative CT contrast agent.[23,24] They are expected to attenuate X rays and become visible in micro-CT images. So far, there have been a number of studies investigating Ag NPs as CT contrast agent.[24]–[26] Nevertheless, the Ag NPs synthesized in these studies had greater average size and relatively broad size distribution with mean size of 21±8 nm. Even though Ag NPs are promising in CT imaging, their ability to absorb X-ray diffraction is inadequate. The Ag–Au alloy structures have been developed in order to reduce the price of products. Recent studies have shown novel and synergic properties of bimetallic NPs compared to single metals. Particularly, the hyaluronic acid modified - Au–Ag material synthesized by Yu Chong et al. showed its effective dual function: radiosensitive tumours by receptor-mediated tumour targeting and generate microenvironment-activated hydroxyl radicals (·OH).[27] In detail, the Au–Ag@HA NPs acted simultaneously as peroxidase and ionizing radiation source, uplifting the formation of •OH and liberation of the poisonous Ag+ in the tumour sites, thus leading to an effective tumour therapeutic outcome. The biocompatible Ag–Au nano alloys hepatoprotective activity against diethylnitrosamine (DEN)-induced liver cancer. Hence, they are a potential candidate for effective nanomedicine development.[28] Recent in-vivo studies on alloy nanoparticles have confirmed their anticancer activity. The study by Vincenzo Amendola et al. showed that Ag–Fe alloy nanoparticles were likely to be removed from the liver while the standard iron oxide contrast agent remained. Therefore, Ag–Fe nano-alloys, in particular, or nano-alloys in general, provide positive prospects to solve the problems of biological durability, contrast efficiency, and the removal of nanomaterials from living organisms.[29] These research results showed that the alloying adds new possibilities for nanomedicine applications. However, controlling size and chemical components of the Ag–Au nanoalloys are still a major challenge.[13] For biomedical uses, the alloy structures ought to be small enough, highly uniform, highly biocompatible and highly dispersive in aqueous environment.

In our study, we fabricated the Ag–Au alloy NPs in organic solvent using substitution reaction between the precusor $Au^{3+}$ and the previously prepared metallic Ag NPs. The effect of the precusor $Au^{3+}$ quantity on morphology and properties of the Ag–Au alloy NPs was also investigated. The as-synthesized NPs were then surface-modified by poly (maleic anhydride-alt-1-octadecene) (PMAO) to form stable colloidal system in aqueous environment. Additionally, in-vitro experiments were conducted to evaluate the potential of the Ag–Au alloy NPs as a contrast agent in imaging diagnosis using computed tomography (CT) technique.

## Results and Discussion

### The formation of Ag NPs

The shape and size of Ag NPs fabricated at different reaction temperatures were analyzed by transmission electron microscope, and shown in Figure 1. As can be seen, the Ag NPs were spherical with clear boundaries and without agglomeration. At 10°C, the obtained Ag NPs had a large size of 10.4±1.9 nm, uneven size distribution, and size error of up to 18.3% (Figure 1A). The synthesis performed at 20°C resulted in Ag NPs with a size of 8.2±1.4 nm and size error of 17% (Figure 1B). When the reaction temperature rose to 30°C, the size of particles was 6.7±0.6 nm. The obtained particles were relatively uniform, size error was reduced to approximately 9% (Figure 1C). The reaction at 40°C produced Ag NPs with a size smaller and more uniform, about 4.3±0.5 nm, and a size error of 11.6% (Figure 1D). Accordingly, the size and uniformity of the Ag NPs depended on the reaction temperature. Higher temperatures resulted in smaller sizes and higher uniformity. These results can be explained as follows: At lower temperatures (10 and 20°C), the complexation reaction between $AgNO_3$ and SOA in ODE solvent occurred slowly, and the Ag crystal seeds appeared after adding the reducing agent about 10 min, as indicated by the color change of the reaction mixture. The nucleation and growth took place at a slow speed, leading to the formation of uneven Ag NPs and wide size distribution. At higher temperatures (30 and 40°C), the Ag crystal seeds were formed immediately when the reducing solution was added to the precursor mixture, both nucleation and growth arose more rapidly. As a consequence, the formed NPs are relatively small and uniform. The dependence of particle size on reaction temperature in our research is similar to a report by Sun et al about the synthesis of Au NPs.[30]

The optical property of Ag NPs was investigated by UV-Vis spectra. The influence of reaction temperature on the optical property of the resulting Ag NPs is presented in Figure 1F. Clearly, there is a surface plasmon resonance (SPR) band typical for silver elements in all samples. The SPR positions of the sample fabricated at 10°C, 20°C, 30°C and 40°C were 402, 401, 399, and 398 nm, respectively. Thence, as the reaction temper-

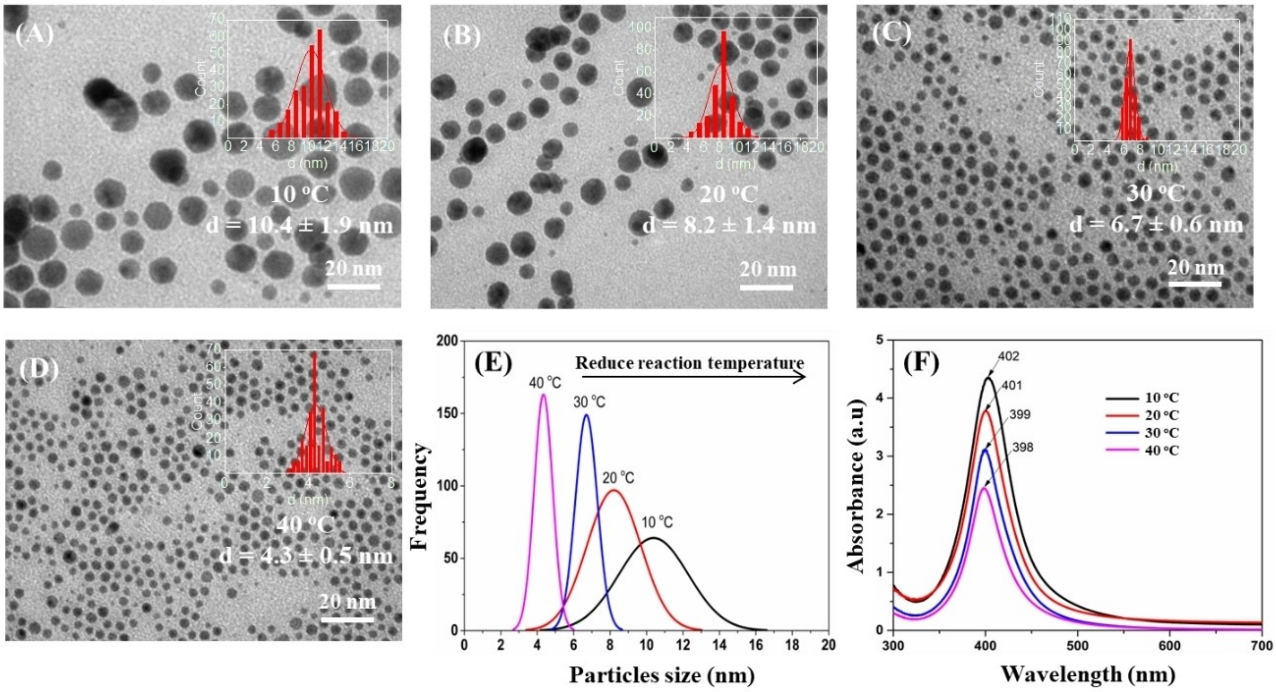

**Figure 1.** TEM images (A–D), size distribution curves (E) and (F) UV-Vis absorption spectra of Ag NPs synthesized at different temperatures.

ature increased from 10 to 40°C, the position of SPR of Ag NPs shifted from 402 to 398 nm, and concurrently, the absorption peaks became narrower. Since the position and shape of SPR absorption bands relied on the shape and size of Ag NPs, the decrease in SPR positions of Ag NPs was a result of the increase in reaction temperature. Our observation is consistent with the published report of Lakshminarayana Polavarapu et al on the synthesis of Ag NPs in organic solvent[31] and that of Meng Chen et al on the fabrication of Ag NPs in aqueous solvent.[32]

## The formation of Ag-Au alloy NPs

The Ag–Au alloy NPs were formed based on the substitution reaction between Ag and $Au^{3+}$ in ODE solvent. Herein, the Ag NPs with a size of 6.7±0.6 nm were used. The influence of the precursor $HAuCl_4.3H_2O$ quantity ranging from 10 to 70 mg on the morphology and properties of Ag–Au alloy NPs was examined. Figure 2 displays the TEM analysis of materials.

The quantity of $HAuCl_4.3H_2O$ influenced the morphology and size of Ag–Au alloy NPs. The sample Ag–Au-10 obtained from 10 mg of $HAuCl_4.3H_2O$ were uneven spherical and quasi-spherical particles with an average size of 8.3±1.5 nm and a size error of 18% (Figure 2B). Using 20 mg of $HAuCl_4.3H_2O$ resulted in uneven spherical Ag–Au-20 particles with a comparative size to the previous sample (8.7±1.6 nm) and a size error of 18.4% (Figure 2C). Formed from 30 mg of $HAuCl_4.3H_2O$, the Ag–Au-30 particles were uniform spheres with an average size increased to 10.8±0.9 nm and size error decreased to 8.3% (Figure 2D). The sample Au–Ag-50 had a relatively even spherical shape with an average size of 14.2±1.0 nm and a size error of 7% (Figure 2E). The sample Ag–Au-70 consisted of nanospheres with an average size of 18.5±1.2 nm and a size error down to 6.5% (Figure 2F). Then, the Ag–Au alloy NPs had greater size than the Ag NPs used (Figure 2A). As the quantity of $HAuCl_4.3H_2O$ was increased from 10 to 70 mg, the average size of the Ag–Au alloy NPs enlarged from 8.3 to 18.5 nm. The trend in changing the size of Ag–Au alloy NPs can be explained as follows: When the quantity of $HAuCl_4.3H_2O$ was low (samples 10 and 20 mg), it produced a moderate amount of Au atoms. Thus, on the Ag seeds, there would be both active sites with Au atoms deposited and empty spaces. On that occasion, the Ostwald ripening effect competed and dominated the deposition reaction.[33]

The formation of Au coating proceeded inhomogeneously among particles in the reaction mixture. Thus, the size of alloy NPs was uneven. When the quantity of $HAuCl_4.3H_2O$ was enough (30–70 mg), the Au formed could prevent the Ostwald ripening, allowing the Au layers on NPs to grow uniformly. Therefore, the Ag–Au alloy NPs had fairly even sizes.

The Au NPs are synthesized by a similar procedure to prepare the referent sample, which had an average size of 14.0±0.9 nm (Figure 2G). It means that under the same conditions, the size of Au NPs was equivalent to that of Ag–Au alloy NPs (sample Ag–Au-50) (Figure 2E). Hence, we chose the sample Ag–Au-50 for further studies.

The formation of the alloy Ag–Au NPs can be described by the redox reaction mechanism. Because the redox potential of $AuCl_4^-$/Au (1.0 V) is higher than that of $Ag^+$/Ag (0.80 V), the Ag of the seeds is oxidized by AuCl4- to form Au by the following reaction:[34]

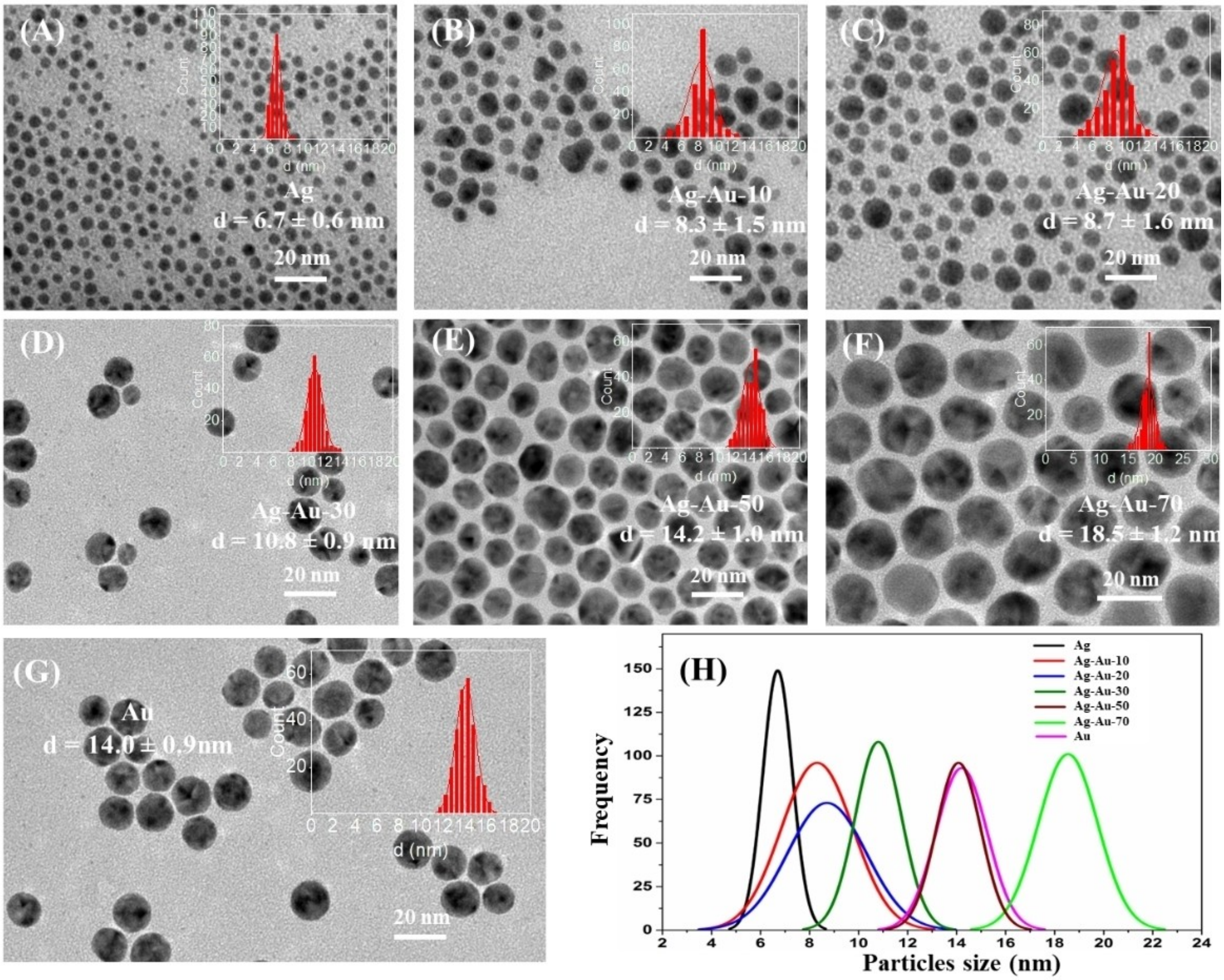

**Figure 2.** TEM images (A–G) and particle size distribution of Ag, Au and Ag–Au alloy NPs synthesized by different quantities of $HAuCl_4.3H_2O$ (H).

$$3\,Ag + AuCl_4^- \rightarrow Au + Cl^- + 3AgCl\downarrow \qquad (1)$$

Later, the Au atoms will deposit on the surface of Ag NPs and interact with the unreacted Ag under suitable conditions to form an alloy.[34] The byproduct AgCl was then discarded by excess concentrated ammonia.

$$AgCl + 2NH_3 \rightarrow [Ag(NH_3)_2]Cl \qquad (2)$$

Through this process, the Ag–Au alloy NPs were separated from AgCl impurities. The X-ray diffraction and energy dispersive X-ray analysis, as presented in Figure 4, supported this conclusion.

The TEM images show that the Ag–Au alloy NPs corresponding to the sample Ag–Au-50 had a spherical shape with an average size of 14.2 ± 1.0 nm (Figure 3A). To figure out the crystal phase of the as-synthesized Ag–Au alloy NPs, the distance between lattice planes (d) was determined by HRTEM and SAED as illustrated in Figure 3B and 3D. HRTEM analysis of Figure 3B showed details about the extended regions between Ag and Au crystals in the alloy. The distinct lattice planes could be seen clearly in HRTEM images, in which the Au crystals were formed alongside the Ag crystals. HRTEM also demonstrated the Ag–Au alloy single-crystal structure, which was created with evenly spaced atoms. In the face-centered cubic (fcc) crystal structure, the distance between the (111) lattice planes was calculated to be 0.235 nm for the gold crystal (JCPDS Card No. 04-0784) and 0.234 nm for the silver crystal (JCPDS Card No. 04-0783). Figure 3C depicts the selected area electron diffraction (SAED) analysis of a single alloy particle, which is spherical. Selected area electron diffraction measurement showed that the Ag–Au alloy NPs were spherical. The bright rings and spots corresponding to the diffraction planes (111), (200) and (311) of the Ag–Au crystal, indicating that the as-synthesized NPs had high crystallization.[35]

XRD, EDX, and TGA measurements were made to acquire a deeper understanding of the crystal structure and elemental composition of the as-synthesized alloy NPs (Figure 4). As shown in the X-ray diffraction pattern, the fabricated sample exhibited distinct and strong peaks demonstrating the formation of NPs. The typical diffraction peaks at 2θ were 38.27,

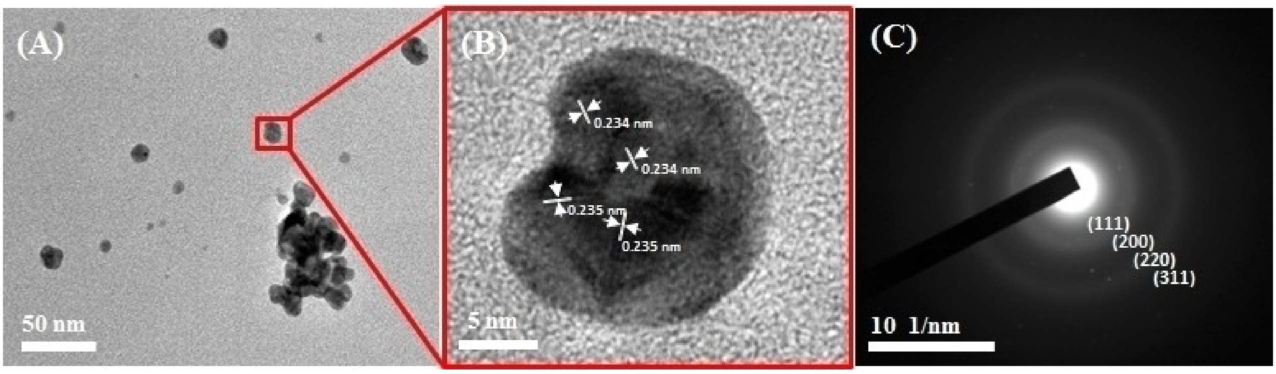

**Figure 3.** TEM images (A), HR-TEM (B) and SEAD images (C) of Ag–Au alloy NPs.

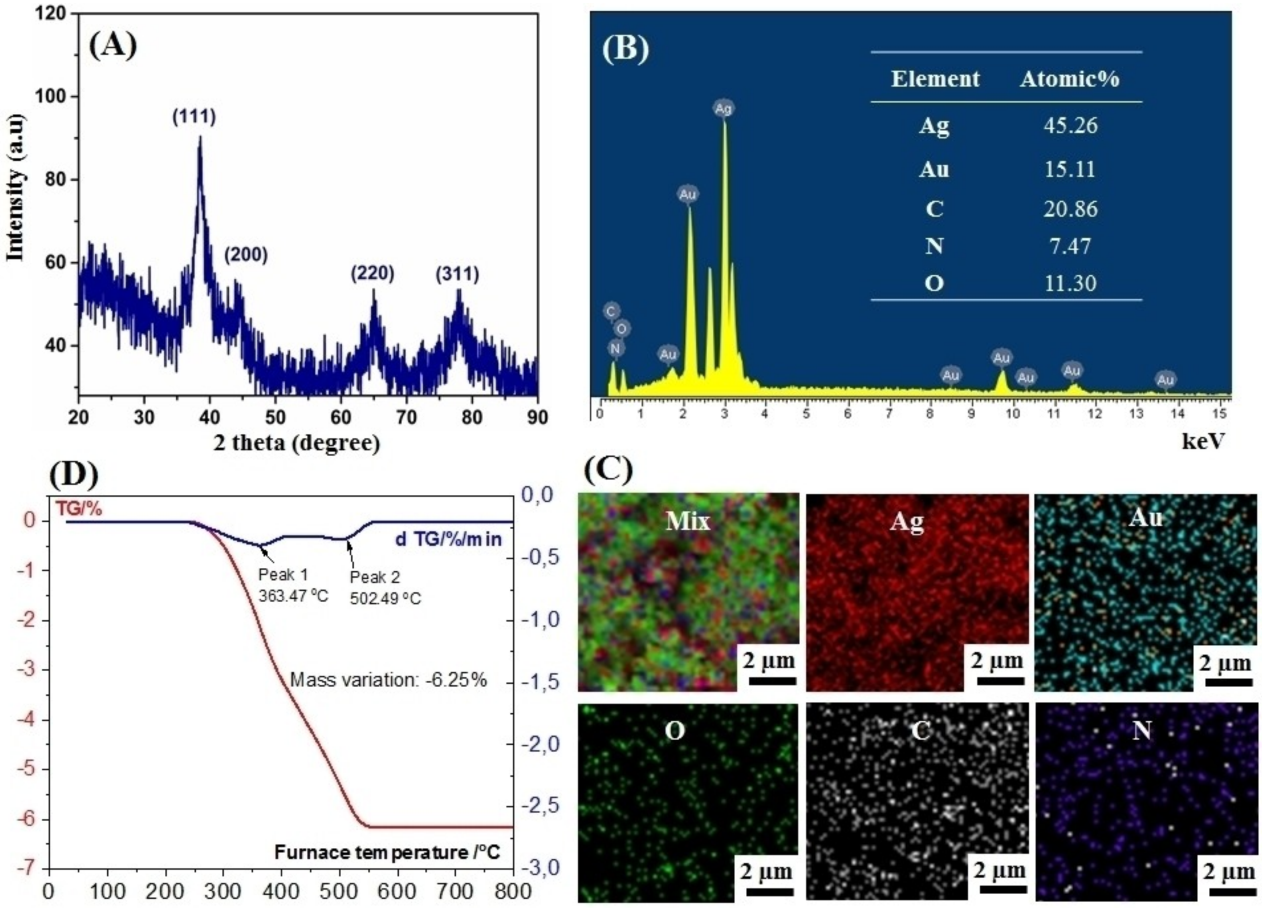

| Element | Atomic% |
|---|---|
| Ag | 45.26 |
| Au | 15.11 |
| C | 20.86 |
| N | 7.47 |
| O | 11.30 |

**Figure 4.** The X-ray diffraction pattern (A), EDX spectrum and elemental percentages of elements (B), EDS elemental mapping (C) and TGA scan of Ag–Au alloy NPs (D).

44.49, 64.73, and 77.76, corresponding to the planes (111), (200), (220), and (311) of the metallic Ag/Au face-centered cubic (fcc) crystals (JCPDS file no. 03–065-8424).[36] Using the Debye–Scherrer expression, the average crystal size of the Ag–Au alloy can be estimated by the measurement of the Full width at half-maximum (FWHM) of the (111) peak, which was found to be 13.36 nm as reported in [37].

The XRD pattern of Ag–Au alloy NPs had a noise background, which was attributed to the surfactant oleate/OLA covering the particle surface. This conclusion was also supported by the EDX spectrum. As presented in Figure 4B, there were typical peaks of Ag and Au elements with high intensity in the EDX spectrum. The atomic percentage of Ag and Au in the alloy was 45.26% and 15.11%, corresponding to the Ag: Au ratio of approximately 3:1. Along with the main elements, the EDX spectrum also showed the other elements such as C, N, and O with lower intensity, whose atomic percentages were 7,57%, 7,84%, and 12,69%, respectively. The reason why the alloy NPs were covered by surfactants (Oleate and OLA) after fabrication was mentioned in previous investigations.[38] From the elemental mapping analysis (Figure 4C), it is obvious that the elements of the Ag–Au alloy NPs are homogeneously distributed in the sample.

According to the TGA analysis (Figure 4D), the alloy sample experienced mass loss in two stages. In the first stage, its mass decreased roughly 3.25% in the temperature range of 230–400°C, corresponding to the loss of organic solvent adsorbed on the surface of particles. At temperatures between 450 and 550°C, the sample lost 3% of its weight as the oleate/OLA surfactant coating broke down. As a result, the Ag–Au alloy NPs were coated by oleate/OLA and accounted for 93.75% of the product by mass.

The optical property of Ag, Au and Ag–Au alloy NPs was studied using UV-Vis absorption spectra, as can be seen in Figure 5.

Research data showed that the color of the Ag–Au alloy solution reflected their composition and microstructure.[39] Based on Mie theory,[40] the characteristic color of Ag, Au, and Ag–Au materials is due to the collective oscillation of delocalized electrons caused by the electromagnetic field of incident light called the surface plasmonic resonance. The change in color of the solutions and the formation of representative absorption peaks suggested the synthesis of alloy NPs with different quantities of $HAuCl_4.3H_2O$. The yellow Ag NP solution had a distinctive absorption peak at 399 nm. The solution was purple, corresponding to the absorption peak at 520 nm. The color of the Ag–Au alloy solution changed from yellow to purple depending on the quantity of $HAuCl_4.3H_2O$ used for synthesis (Figure 5A). The color change was revealed by the shift of maximum absorption as the quantity of $HAuCl_4.3H_2O$ increased (Figure 5B). The samples Ag–Au-10 and Ag–Au-20 showed broadened absorption peaks at 427 and 443 nm, respectively. This observation could be attributed to the low concentration of precursor $HAuCl_4.3H_2O$, thus the Au atoms were formed in a small amount. In this case, the alloy mainly consisted of Ag metal, hence its SPR peak did not shift significantly compared to that of Ag NPs. Concurrently, the uneven particle size might also cause the broadening of the peak. The samples Ag–Au-30 and Ag–Au-50 gave maximum absorption at 487 and 520, correspondingly, with a relatively narrow SPR peak. In this instance, the maximum absorption strongly shifted away from the short wavelengths of Ag NPs and gradually approached that of Au NPs. The increase in the amount of $HAuCl_4.3H_2O$ raised the composition of Au in the alloy, enlarged the average particle size, and enhanced the uniformity. There was a shift of SPR peak toward the long wavelength (522 nm) in the sample Ag–Au-70, even higher than that of Au NPs (520 nm). It means that by increasing the percentage of Au, the size of Ag–Au alloy NPs became greater than the initial Au (as proved by TEM images in Figure 2). Simultaneously, the SPR effect among Ag and Au atoms was enforced by the rise of Au composition. To sum up, as the quantity of $HAuCl_4.3H_2O$ increased in the investigated range (10 – 70 mg), the SPR position of Ag–Au alloy shifted from 427 to 522 nm. The sample formed by using 70 mg of $HAuCl_4.3H_2O$ owned the strongest SPR shift, which was 123 nm compared to that of Ag NPs due to the powerful plasmon binding effect among Ag and Au atoms in alloy.[36] Under the synergistic effect of Ag and Au composition in the alloy and particle size, the Ag–Au alloy NPs exhibited SPR peaks over a wide range of UV-Vis spectra. Each sample showed only one absorption peak locating between the SPR peaks of single Ag NPs and single Au NPs. The sample Ag–Au-70 was exceptional since it had a slight shift toward the long wavelength region compared to Au NPs because of its larger size. Since a physical mixture consisting of Ag and Au elements should present two corresponding SPR peaks. It clarifies that the obtained NPs were an alloy of Ag and Au, but not a mixture. A similar observation was reported in previous studies.[36]

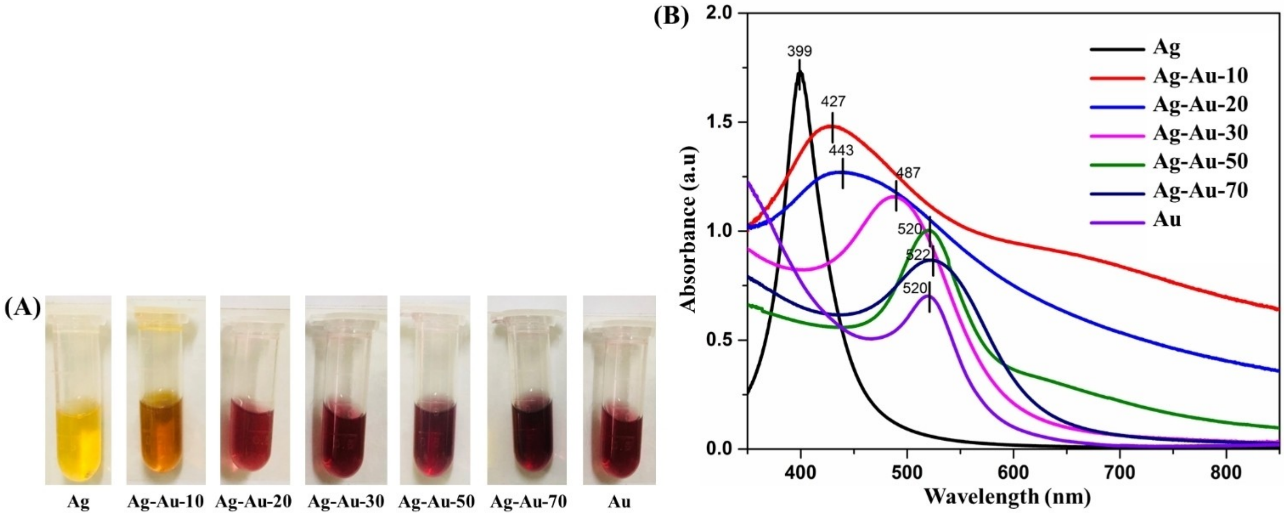

**Figure 5.** The solution of the samples (A), and their UV-Vis spectra (B) of Ag, Ag–Au NPs (with different quantities of $HAuCl_4.3H_2O$) and Au NPs dispersed in n-hexane.

### *Phase transfer of Ag, Au, and Ag-Au NPs into aqueous solvent*

In this study, the Ag, Au, and Ag–Au alloy NPs were fabricated in organic solvent with the participation of oleate and OLA as surfactants. As a result, the particle surface was covered by oleate/OLA, rendering the particles dispersible in organic solvents.[41] However, for biomedical application, the NPs must be dispersible in an aqueous solvent. As a result, PMAO was used to transfer the phase of the Ag (the seed, 6.7 ± 0.6 nm), Au (14.0 ± 0.9 nm), and Ag–Au (14.2 ± 1.0 nm) NPs from organic solvent to water as illustrated in Figure 6A.

In short, the phase transfer mechanism of NPs by PMAO is as follows: The PMAO molecules consist of both hydrophobic and hydrophilic functions. The hydrophobic tail is hydrocarbon that forms bonds with the hydrocarbon of oleate/OLA on the particle surface. The hydrophilic head is anhydride groups that are hydrolyzed in alkaline solution to form carboxylate groups, supporting the dispersion of particles in an aqueous environment.[41]

It is shown that the Ag, Ag–Au, and Au NPs before being coated by PMAO were dispersible in an n-hexane solvent (Figure 5A). After encapsulation by PMAO, the nanoparticle surface becomes hydrophilic and dispersible in an aqueous solution. The color of solutions before and after phase transfer changed negligibly (Figure 6B). This result was also proved by UV-Vis spectra of the Ag, Ag–Au, and Au NPs after phase transfer. The corresponding maximum absorption positions were at 399, 520, and 520 nm, which changed insignificantly compared to those of samples before phase transfer (Figure 6C).

The formation of PMAO coating on the nanoparticle surface after phase transfer was examined by Fourier Transform Infrared (FT-IR) (Figure 6D). We can see that the alloy NPs after phase transfer (Ag–Au@PMAO) gave a broad maximum absorption range at wave number of 3451 cm$^{-1}$ that was assigned to the vibration of OH in water molecules absorbed onto PMAO coating. The absorption peaks at wave numbers 2924 cm$^{-1}$ and 2853 cm$^{-1}$ indicate the symmetric and asymmetric vibration of the C–H bond in the $CH_2$ group that appeared in both samples. There was a peak at 1631 cm$^{-1}$ characterized for the N–H bond of OLA in the sample before phase transfer. Moreover, two absorption peaks at 1450 cm$^{-1}$ and 1384 cm$^{-1}$ were present in the sample after phase transfer which were attributed to symmetry and asymmetry vibration of the carboxylate group of PMAO.

### *In vitro cytotoxicity results*

Given the potential for biological applications, assessing the cytotoxicity of Ag–Au@PMAO is crucial for evaluating its biocompatibility. Therefore, an SRB assay was conducted on

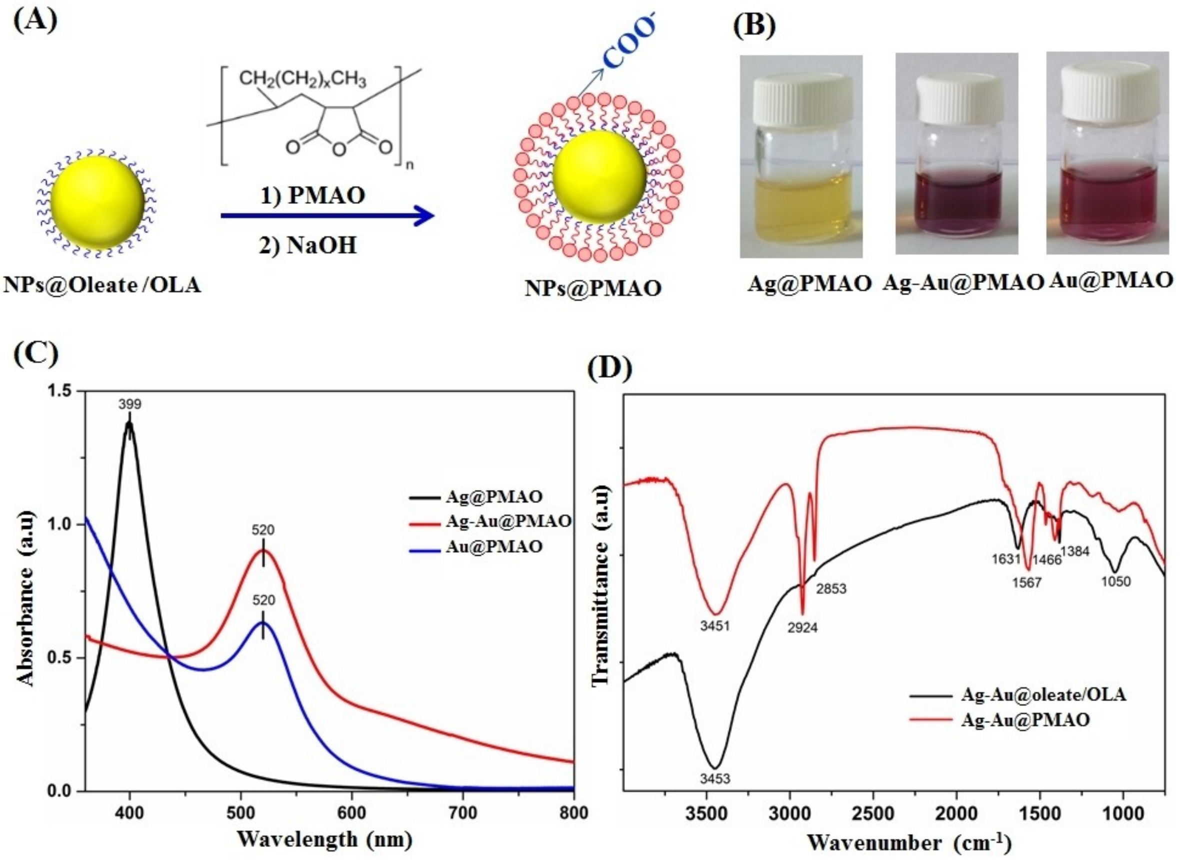

**Figure 6.** Illustration of phase transfer mechanism using PMAO (A), photo of solutions (B) and UV-Vis spectra (C) of Ag, Ag–Au and Au NPs after being covered by PMAO, FT-IR spectra of oleate/OLA and PMAO encapsulated Ag–Au alloy NPs.

Vero cells, a normal monkey kidney cell line, using a range of Ag–Au@PMAO concentrations from 6.25 μg/mL to 100 μg/mL. Ellipticine and DMSO served as positive and solvent controls, respectively (Figure 7a). As anticipated, the control conditions yielded expected results: 100% cell survival in the DMSO-treated group and complete cancer cell death in the Ellipticine-treated group (Figure 7a). Within the investigated concentration range of 6.25 to 100 μg/mL, Ag–Au@PMAO demonstrated minimal impact on Vero cell survival rate or morphology (Figure 8). Although a slight light influence was observed at higher concentrations (50 and 100 μg/mL), cell death did not exceed 50%, resulting in an $IC_{50}$ for Ag–Au@PMAO on Vero cells exceeding 100 μg/mL (Figure 7b). This finding indicates a low degree of toxicity towards the Vero cell line.

The morphological changes in Vero cells exposed to Ag–Au@PMAO were evaluated at various concentrations, ranging from 6.25 μg/mL to 100 μg/mL. As depicted in Figure 8, no discernible alterations in cell shape were observed throughout the investigated concentration range. Prior studies have demonstrated the cytotoxicity of individual Ag, Au materials. For instance, Vero cells exposed to 50 μg/mL of Ag for 24 hours exhibited a 25% reduction in viability.[42] Conversely, Au nanoparticles have been shown to have minimal impact on the viability of cultured Vero cells.[42] Interestingly, treatment with very low (5 μg/mL) or very high (100 μg/mL) doses of Au-NPs resulted in a transient decrease in Vero cell mitochondrial function, but the cells recovered after 48 hours. These findings suggest that the formation of the Ag–Au alloy and subsequent encapsulation with PMAO polymer have significantly reduced the material's toxicity compared to individual Ag components. Furthermore, the observed biocompatibility of Ag–Au@PMAO with normal Vero cells, as evidenced by the present data, paves the way for its potential application in enhancing CT quality. A similar observation was reported in our previous studies.[42,43] Poly(maleic anhydride-alt-1-octadecene) (PMAO) stands out as a preferred inert organic material for surface modification. Its unique properties enhance the stability and biocompatibility of nanoparticles (NPs).[45] PMAO coating effectively prevents NP aggregation while introducing many hydrophobic alkyl chains onto the NP surface. These chains establish strong associations with hydrocarbon ligands on the NPs via hydrophobic van der Waals interactions.[46] The repeating unit of PMAO features maleic anhydride groups that readily hydrolyze to carboxylic groups, enabling dispersion of the composite NPs in water or polar solvents. Additionally, these carboxylic groups serve as versatile anchors for further conjugation to biomolecules or ligands.[47] The highly reactive anhydride groups of PMAO offer additional potential for grafting functional molecules onto the main polymeric chain.[48] However, further investigations are warranted to comprehensively understand the cellular uptake,

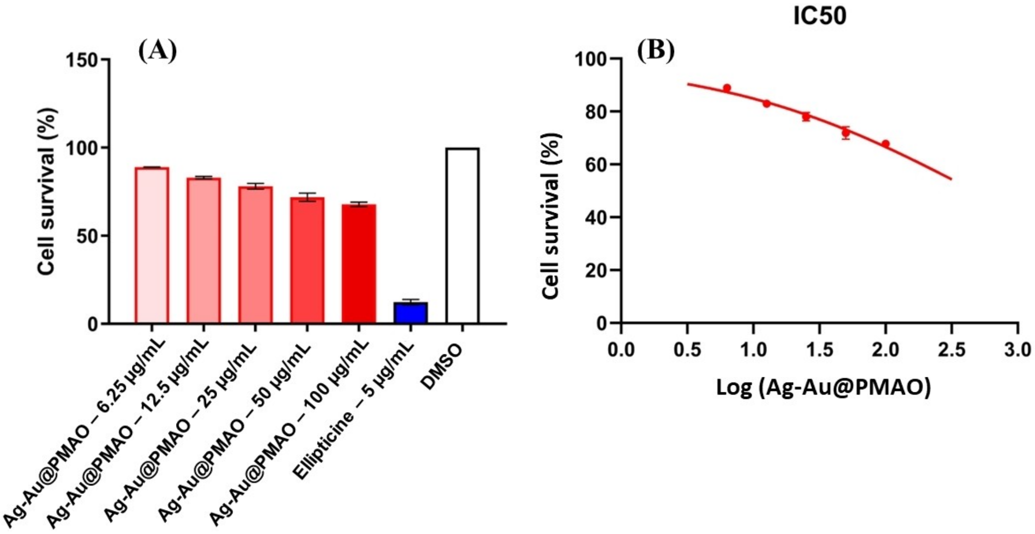

**Figure 7.** Cytotoxicity of Ag–Au@PMAO on Vero. (a) Percentage of cell survive of samples incubated with Ag–Au@PMAO (6.25–12.5–25–50–100 μg/mL); DMSO and Ellipticine (5 μg/mL); and (b) $IC_{50}$ curve with log concentration of Ag–Au@PMAO. Graphs were obtained by using GraphPad and data was presented as mean ± SD.

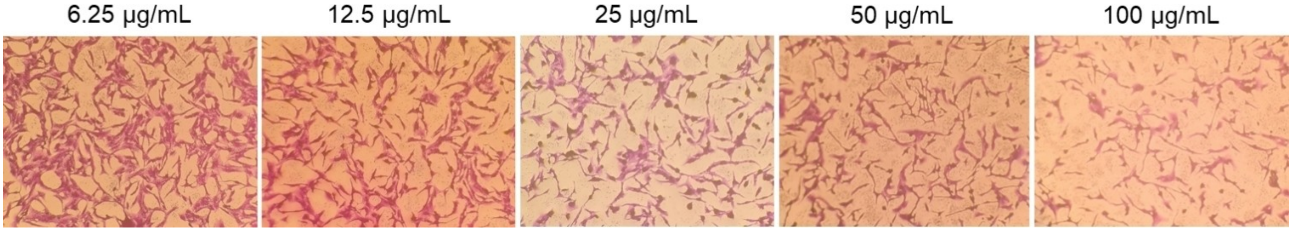

**Figure 8.** Vero cell treated with a range of concentration of Ag–Au@PMAO. Microscope images were taken with objective lens: 10X.

organ accumulation, and mechanisms of cancer cell targeting and killing associated with Ag–Au@PMAO.

### CT Evaluation of CT imaging contrast agent

The utilization of Ag–Au alloy NPs as CT contrast agents is noteworthy. Due to high atomic numbers, the alloy NPs can induce stronger X-ray attenuation than iodine-based complexes. To further investigate the potential of these NPs, the X-ray attenuation property of Ag–Au@PMAO with different quantities of $HAuCl_4.3H_2O$ at a concentration of 3 mg/mL was examined. The intensity of X-ray attenuation in the various samples was assessed using digital CT scans. This evaluation was performed in a standard display program, eFilm workstations software (Merge Healthcare, Chicago, IL, USA). A consistent region of interest (ROI) was chosen within the CT image of each sample for accurate comparison. The contrast intensity changes in the materials with varying Ag/Au ratios were measured in Hounsfield units (HU).

Figure 9a vividly illustrates a statistically significant difference ($P < 0.05$) in X-ray attenuation between the Ag–Au alloys with varying Au content. Here, a bar graph could effectively showcase the Hounsfield unit (HU) signal intensity for each sample. We observe a clear upward trend, revealing that increasing the Au content within the Ag–Au alloy leads to a linear increase in X-ray attenuation. Notably, the HU signal intensity of the Ag–Au-50 sample is a remarkable 11.7 times higher than that of the Ag–Au-10 sample. This substantial enhancement in X-ray attenuation with increasing Au content is evident in the figure. However, when the Au content further increases from 50 mg (Ag–Au-50) to 70 mg (Ag–Au-70), corresponding to Ag : Au ratios of 3.83 : 1 and 1.88 : 1, respectively, only statistically significant differences ($P < 0.01$) remain in X-ray attenuation. This apparent plateauing effect can be attributed to reaching an optimal Ag : Au ratio for the alloy structure. At this point, the size factor of the nanoparticles starts to play a more dominant role in influencing X-ray attenuation than the absolute Au content. Due to its smaller size compared to the Ag–Au-70 sample, the Ag–Au-50 sample exhibits a larger surface area, a well-established relationship.[49] This aligns with observations by Sun et al., who reported higher X-ray attenuation in smaller Au nanoparticles due to their enhanced surface-to-volume ratio.[50] This can be directly observed in our CT images, where the Ag–Au-70 sample displays only a negligible increase in contrast signal compared to the Ag–Au-50 sample. The Hounsfield units (HU) only increase from 73.9 to 81.1 (a mere 9.74 % increase). Taking these findings together with the previously obtained TEM measurements, we opted for the Ag–Au-50 sample for further investigation.

To further investigate the potential of these NPs, the X-ray attenuation property of Ag–Au@PMAO at a concentration of 5 mg/mL was examined. Other Au@PMAO samples at the same concentration were used as the control. Figure 10A depicts the clear CT imaging contrast for both samples at higher concentrations than 3 mg/mL. As the concentration of material raised to 1–5 mg/mL, the radiopaque (X-ray attenuation) increased, corresponding to the increase in CT contrast of both samples. The CT image intensity increased linearly, consistent with the increase of Hounsfield intensity value for both samples. Same as

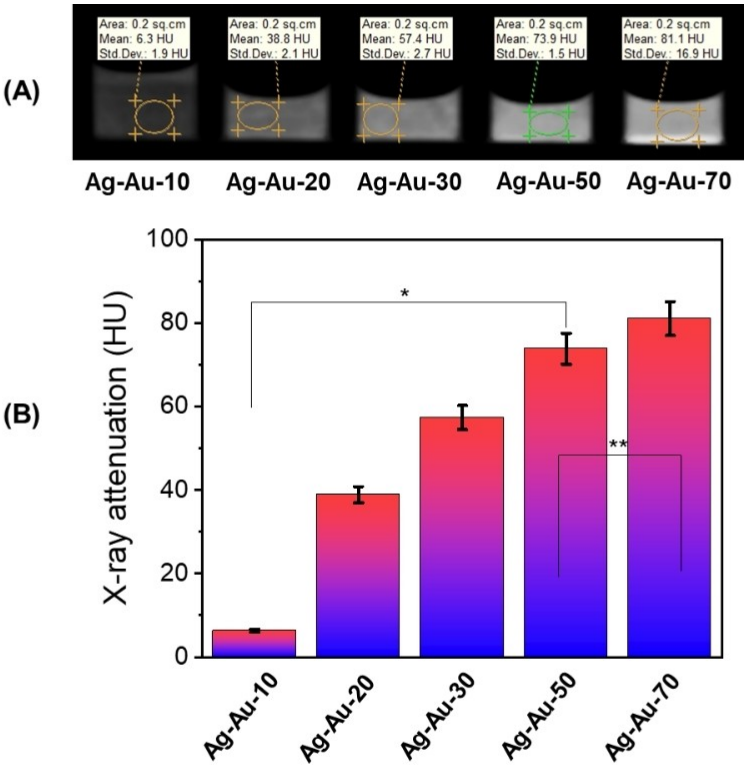

**Figure 9.** CT images of the nano Ag–Au at different ratios of Ag/Au alloy (A), and respective X-ray attenuation intensity (B).

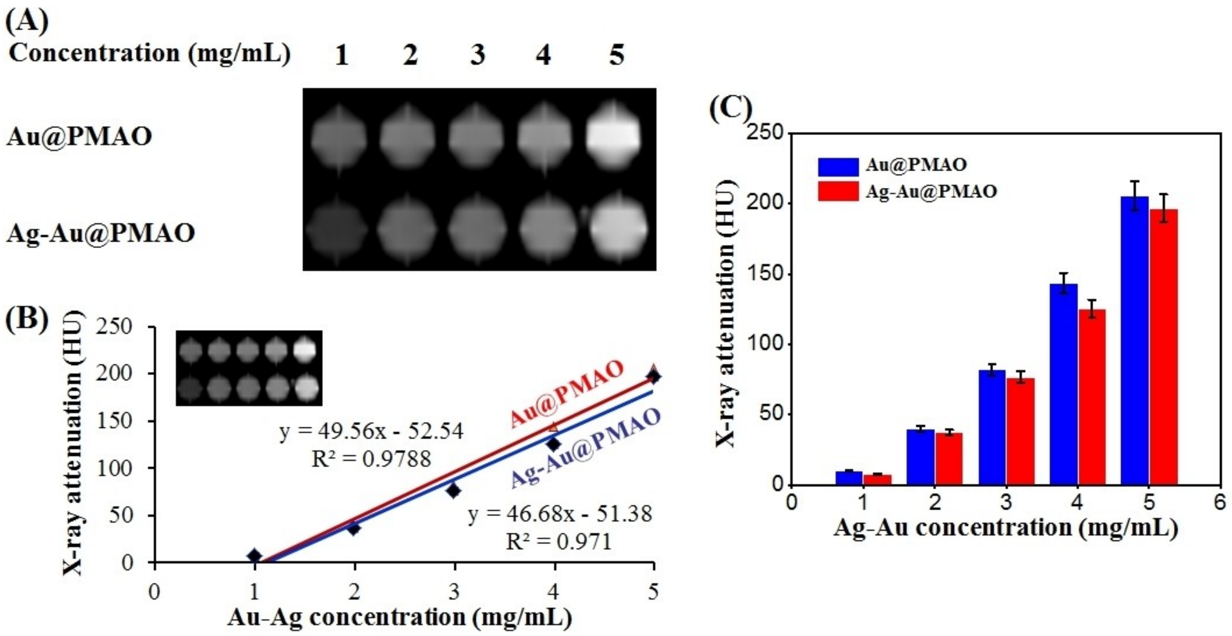

**Figure 10.** CT images of the nano Au@PMAO and Ag–Au@PMAO at different concentration (A), linear plot of the corresponding Hounsfield unit (B) and respective X-ray attenuation intensity (C).

expectations, quantification using an average grayscale table revealed a linear relationship between the observed CT contrast and the concentration of NPs, $R^2 = 0.978$ for nano Au@PMAO and $R^2 = 0.971$ for Ag–Au@PMAO nanoalloy (Figure 10B). As the concentration of material increased from 1 to 5 mg/mL, Hounsfield (HU) signal intensity rose from 7.5 HU up to 196.8 HU (approximately 26.24 times) for the nano Ag–Au@PMAO and from 9.9 HU to 205.7 HU (about 20.78 times) for the nano Au@PMAO (Figure 10C). Therefore, the nano Ag–Au@PMAO gave a CT imaging contrast signal equivalent to Au@PMAO at the studied concentration.

Comparision of the X-ray attenuation of Ag–Au@PMAO and Au@PMAO at concentration of 3 mg/mL with water, we can observe the X-ray attenuation of the materials. Results are presented in Figure 11.

It is found that the Hounsfield intensity signal for water was −38.9 HU, while that of Au@PMAO and Ag–Au@PMAO increased to 82.7 HU and 78.3 HU, respectively. Comparing the Hounsfield signal of the Ag–Au alloy NPs to that of Au NPs and iodine complexes as contrast agents, the value of Ag–Au alloy NPs in this study was not much different. For instance, in the study of Yuxi C. Dong et al, as the concentration of Au NPs changed from 0.5 to 10 mg/mL, the corresponding Hounsfield signal intensity increased from 30 HU to 270 HU.[18] A study by Mohammed Ali Dheyab et al showed that, to reach Hounsfield signal intensity of 178 HU, the concentration of Au NPs and iodine (in the commercial drug Omnipaque) had to be 2.3 mg/mL and 7.2 mg/mL, respectively.[51] Hence, preliminary in-vitro experiments suggested that the PMAO-modified Ag–Au alloy NPs could be used as a potential CT contrast agent.

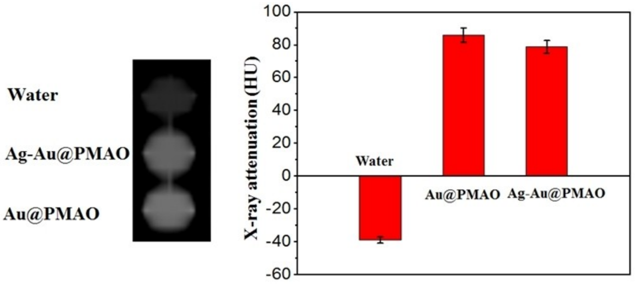

**Figure 11.** The X-ray attenuation intensity of nano Au@PMAO and Ag–Au@PMAO at concentration of 3 mg/mL and that of water.

## Conclusions

The Ag–Au alloy NPs were synthesized successfully in an organic solvent. The quantity of $HAuCl_4.3H_2O$ influenced the morphology and properties of the alloy materials. Characterization result showed that the Ag–Au alloy NPs with a size of 14.2 ± 1.0 nm, SPR maximum absorption peak at 520 nm, and Ag: Au ratio of approximately 3:1 were appropriate for biomedical applications. The Ag–Au solutions after phase transfer using PMAO reached high durability, stability and non-toxic to the Vero healthy cell line. *In-vitro* CT images indicated a good X-ray absorption coefficient. The hounsfield unit (HU) was increased significantly (196.8 HU at 5 mg/mL), suggesting that Ag–Au alloy was potentially CT contrast agent whereas the X-ray attenuation correlated linearly to the concentration of Ag–Au NPs. Our findings expanded the potential uses of Ag–Au alloy NPs in biomedicine, particularly for imaging diagnosis employing CT imaging technology.

## Acknowledgements

This research was supported by Project of the TNU-University of Sciences in Vietnam under Grant number CS2021-TN06-17.

## Conflict of Interests

The authors declare no conflict of interest.

## Data Availability Statement

The data that support the findings of this study are available on request from the corresponding author. The data are not publicly available due to privacy or ethical restrictions.

**Keywords:** Ag–Au alloy · CT imaging applications · poly (maleic anhydride-alt-1-octadecene) (PMAO) · thermal decomposition · X-ray attenuation property

[1] M. A. Dheyab, A. A. Aziz, P. M. Khaniabadi, M. S. Jameel, N. Oladzadabbasabadi, S. A. Mohammed, R. S. Abdullah, B. Mehrdel, *Int. J. Mol. Sci.* **2022**, *23*, 7400.

[2] W. I. Abdel-Fattah, G. W. Ali, *J. Appl. Biotechnol. Bioeng.* **2018**, *5*, 43–46.

[3] A. J. Haes, R. P. Van Duyne, *Expert Rev. Mol. Diagn.* **2004**, *4*, 527–537.

[4] G. M. Raghavendra, T. Jayaramudu, K. Varaprasad, R. Sadiku, S. S. Ray, K. Mohana Raju, *Carbohydr. Polym.* **2013**, *93*, 553–560.

[5] R. Salomoni, P. Léo, A. F. Montemor, B. G. Rinaldi, M. F. A. Rodrigues, *Nanotechnol. Sci. Appl.* **2017**, *10*, 115–121.

[6] C. Cabal, D. Darias, E. González, and A. Musacchio, *Biotecnol. Apl.* **2013**, *30*, 172–177.

[7] L. Li, H. M. F. Jing Cai, Yu Qing Miao, *Int. J. Mol. Sci.* **2018**, *19*, 4049.

[8] N. Lee, D. Yoo, D. Ling, M. H. Cho, T. Hyeon, J. Cheon, *Chem. Rev.* **2015**, *115*, 10637–10689.

[9] H. K. Pannu, R. E. Thompson, J. Phelps, C. A. Magee, E. K. Fishman, *Acad. Rad.* **2005**, *12*, 576–584.

[10] C. E. M. ter Voert, R. Y. N. Kour, B. C. J. van Teeffelen, N. Ansari, K. S. Stok, *J. Anat.* **2020**, *237*, 1062–1071.

[11] M. H. K. Hoffmann, *Contrast Agent Application and Protocols.* **2008**.

[12] B. Mruk, *Polish J. Radiol.* **2016**, *81*, 157–165.

[13] S. Ahmed, G. Baijal, R. Somashekar, S. Iyer, V. Nayak, *Int. J. Nanomed.* **2021**, *16*, 7103–7121.

[14] M. Oumano, L. Russell, M. Salehjahromi, L. Shanshan, *N. Sinha, W. Ngwa, H. Yu, Appl. Clin. Med. Phys.* **2021**, *22*, 337–342.

[15] R. D. Ross, L. E. Cole, J. M. R. Tilley, R. K. Roeder, *Chem. Mater.* **2014**, *26*, 1187–1194.

[16] I. Takeuchi, S. Nobata, N. Oiri, K. Tomoda, K. Makino, *Bio-Med. Mater. Eng.* **2017**, *28*, 315–323.

[17] I. Takeuchi, H. Onaka, K. Makino, *Bio-Med. Mater. Eng.* **2018**, *29*, 205–215.

[18] Y. C. Dong, M. Hajfathalian, P. S. N. Maidment, J. C. Hsu, P. C. Naha, S. S. Mohamed, M. Breuilly, J. Kim, P. Chhour, P. Douek, H. I. Litt, D. P. Cormode, *Sci. Rep.* **2019**, *9*, 14912.

[19] T. H. L. Nghiem, T. N. Le, T. H. Do, T. T. D. Vu, Q. H. Do, H. N. Tran, *Nanoparticle Res.* **2013**, *15*, 2091.

[20] X. H. Vu, M. Levy, T. Barroca, H. N. Tran, E. Fort, *Nanotechnology.* **2013**, *24*, 325501.

[21] N. T. Dung, N. T. N. Linh, D. L. Chi, N. T. H. Hoa, N. P. Hung, N. T. Ha, P. H. Nam, N. X. Phuc, Le T. Tam, Le T. Lu, *RSC Adv.* **2021**, *11*, 13458–13465.

[22] M. Sabela, S. Balme, M. Bechelany, J. M. Janot, K. Bisetty, *Adv. Eng. Mater.* **2017**, *19*, n1700270.

[23] S. Ramesh, M. Grijalva, A. Debut, B. G. De La Torre, F. Albericio, L. H. Cumbal, *Biomater. Sci.* **2016**, *4*, 713–1725.

[24] J. Zou, M. Hannula, S. Misra, H. Feng, R. H. Labrador, A. S. Aula, J. Hyttinen, I. Pyykkö, *J. Nanobiotechnol.* **2015**, *13*, 1–9.

[25] E. M. Lee, E. M. Lee, J. Lee, Y. Kim, K. S. Yi, J. Cho, J. Kim, J. M. An, D. Lee, S. J. Kim, E. An, Y. J. Hong, H. Jo, S. H. Lee, Y. Jung, C. H. Choi, J. S. Kang, J. Hur, D. Kim, *ACS Biomater. Sci. Eng.* **2020**, *6*, 4390–4396.

[26] Z. Li, L. Tian, J. Liu, W. Qi, Q. Wu, H. Wang, M. C. Ali, W. Wu, H. Qiu, *Adv. Healthcare Mater.* **2017**, *6*, 1700413.

[27] Y. Chong, J. Huang, X. Xu, C. Yu, X. Ning, S. Fan, Z. Zhang, *Bioconjugate Chem.* **2020**, *31*,1756–1765.

[28] T. Shanmugasundaram, M. Radhakrishnan, V. Gopikrishnan, K. Kadirvelu, R. Balagurunathan, *Nanoscale.* **2017**, *9*, 16773–16790.

[29] V. Amendola, A. Guadagnini, S. Agnoli, D. Badocco, P. Pastore, G. Fracasso, M. Gerosa, F. Vurro, A. Busat, P. Marzola, *J. Colloid Interface Sci.* **2021**, *596*, 332–341.

[30] S. Peng, Y. Lee, C. Wang, H. Yin, S. Dai, S. Sun, *Nano Res.* **2008**, *1*, 229–234.

[31] L. Polavarapu, L. M. Liz-Marzán, *Nanoscale.* **2013**, *5*, 4355–4361.

[32] H. J. Li, A. Q. Zhang, Y. Hu, L. Sui, D. J. Qian, M. Chen, *Nanoscale Res. Lett.* **2012**, *7*, 1–13.

[33] D. M. Mott, S. Maenosono, N. T. T. Trang, T. T. Thuy, K. Higashimine, *Plasmonics.* **2013**, *8*, 1177–1184.

[34] Q. Zhang, J. Y. Lee, J. Yang, C. Boothroyd, J. Zhang, *Nanotechnology* **2007**, *18*, 245605.

[35] E. K. Fodjo, A. Canlier, C. Kong, A. Yurtsever, P. L. A. Guillaume, F. T. Patrice, M. Abe, T. Tohei, A. Sakai, *Adv. Nanoparticles.* **2018**, *7*, 37–45.

[36] T. T. Ha Pham, N. D. Dien, X. H. Vu, *SC Adv.* **2021**, *11*, 21475–21488.

[37] D. H. A. O. M. Ozkendir, E. Cengiz, E. Yalaz, O. Sogut, B. N. Thammajak, *J. Electron Spectrosc. Relat. Phenom.* **2016**, *209*, 53–61.

[38] N. T. N. Linh, N. T. Dung, L. T. T. Tam, L. T. Tam, N. P. Hung, N. D. Vinh, N. T. Ha, P. H. Nam, L. V. Thanh, N. V. Dong, L. G. Nam, N. V. Dang, N. X. Phuc, L. D. Tung, N. T. K. Thanh, L. T. Lu, *New J. Chem.* **2023**, *47*, 4052–4067.

[39] L. Sun, W. Luan, Y. J. Shan, *Nanoscale Res. Lett.* **2012**, *7*, 1–6.

[40] K. M. Mayer, J. H. Hafner, *Chem. Rev.* **2011**, *111*, 3828–3857.

[41] N. T. N. Linh, L. T. Tam, H. M. Nguyet, N. T. Dung, N. H. Du, L. T. T. Tam, P. H. Nam, N. D. Vinh, N. T. Vuong, N. D. Quang, L. T. Lu, *Vietnam J. Chem.* **2021**, *59*, 431–439.

[42] J. L. Speshock, L. K. Braydich-Stolle, E. R. Szymanski, and S. M. Hussain, *Nanoscale Res. Lett.* **2011**, *6*, 1–7.

[43] N. T. Dung, N. T. N. Linh, D. L. Chi, c N. T. H. Hoa, N. P. Hung, N. T. Ha, P. H. Nam, N. X. Phuc, L. T. Tam, L. T. Lu, *RSC Adv.* **2021**, *11*, 13458–13465.

[44] P. H. Nam, L. T. Lu, P. H. Linh, D. H. Manh, L. T. T. Tam, N. X. Phuc, P. T. Phong, I. J. Lee, *New J. Chem.* **2018**, *42*, 14530–14541.

[45] R. D. Corato, A. Quarta, P. Piacenza, A. Ragusa, A. Figuerola, R. Buonsanti, R. Cingolani, L. Manna, T. Pellegrino, *J. Mater. Chem.* **2008**, *18*, 1991–1996.

[46] J. Qin, Y. S. Jo, M. Muhammed, *Angew. Chem.* **2009**, *121*, 7985–7989.

[47] T. Pellegrino, L. Manna, S. Kudera, T. Liedl, D. Koktysh, A. L. Rogach, S. Keller, J. Radler, G. Natile, W. J. Parak, *Nano Letter.* **2006**, *4*, 703–707.

[48] W. W. Yu, E. Chang, J. C. Falkner, J. Zhang, A. M. Al-Somali, C. M. Sayes, J. Johns, R. Drezek, V. L. Colvin, *J. Am. Chem. Soc.* **2007**, *129*, 2871–2879.

[49] V. Rotello, *Nanostructure Sci. Technol. Springer.* **2004**.

[50] X. Chenjie, G. A. Tung, S. Shouheng, *Chem. Mater.* **2008**, *20*, 4167–4169.

[51] M. A. Dheyab, A. A. Aziz, M. S. Jameel, P. M. Khaniabadi, A. A. Oglat, *Appl. Sci.* **2020**, *10*, 7020.

Manuscript received: December 26, 2023
Revised manuscript received: January 3, 2024
Accepted manuscript online: January 5, 2024
Version of record online: ■■, ■■

# RESEARCH ARTICLE

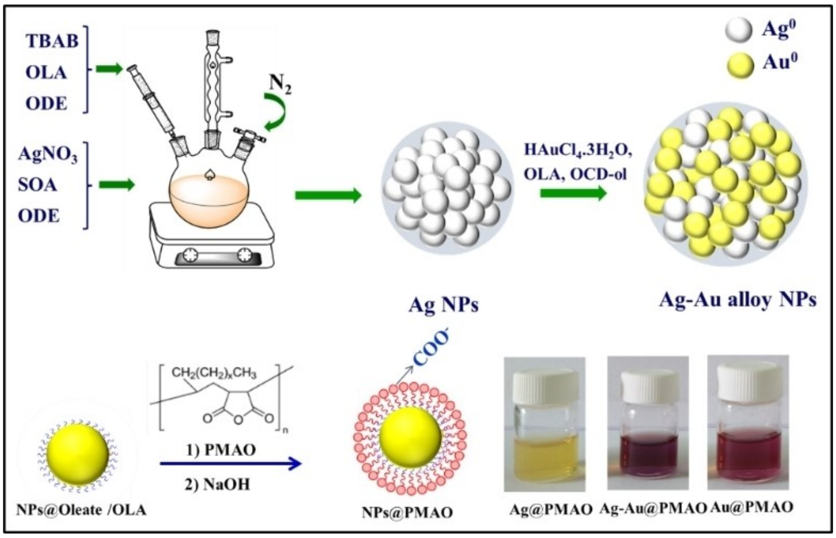

*Dr. N. T. N. Linh, Dr. L. T. Tam*, Prof. N. H. Du, Prof. N. D. Vinh, Prof. P. T. H. Tuyet, Dr. B. M. Quy, C. T. An, N. T. Suong, Dr. N. T. H. Hoa, Dr. L. T. Lu*

1 – 12

**Synthesis and Properties of Ag-Au Alloy Nanoparticles with Controlled Composition for Computed Tomography Imaging Applications**

In this study, Ag–Au alloy NPs were synthesized successfully in an organic solvent. The quantity of HAuCl$_4$.3H$_2$O influenced the morphology and properties of the alloy materials. The Ag–Au solutions after phase transfer using poly (maleic anhydride-alt-1-octadecene) reached high durability, stability and non-toxic to the Vero healthy cell line. *In-vitro* CT images indicated a good X-ray absorption coefficient. Our findings expanded the potential uses of Ag–Au alloy NPs in biomedicine, particularly for imaging diagnosis employing CT imaging technology.